

OPENING THE 21CM EOR WINDOW: MEASUREMENTS OF FOREGROUND ISOLATION WITH PAPER

JONATHAN C. POBER¹, AARON R. PARSONS¹, JAMES E. AGUIRRE², ZAKI ALI¹, RICHARD F. BRADLEY^{3,4,5}, CHRIS L. CARILLI⁶, DAVE DEBOER⁷, MATTHEW DEXTER⁷, NICOLE E. GUGLIUCCI⁵, DANIEL C. JACOBS⁸, PATRICIA J. KLIMA⁴, DAVE MACMAHON⁷, JASON MANLEY⁹, DAVID F. MOORE², IRINA I. STEFAN¹⁰, WILLIAM P. WALBRUGH⁹

Draft version May 6, 2013

ABSTRACT

We present new observations with the Precision Array for Probing the Epoch of Reionization (PAPER) with the aim of measuring the properties of foreground emission for 21cm Epoch of Reionization experiments at 150 MHz. We focus on the footprint of the foregrounds in cosmological Fourier space to understand which modes of the 21cm power spectrum will most likely be compromised by foreground emission. These observations confirm predictions that foregrounds can be isolated to a “wedge”-like region of 2D (k_{\perp} , k_{\parallel})-space, creating a window for cosmological studies at higher k_{\parallel} values. We also find that the emission extends past the nominal edge of this wedge due to spectral structure in the foregrounds, with this feature most prominent on the shortest baselines. Finally, we filter the data to retain only this “unsmooth” emission and image specific k_{\parallel} modes of it. The resultant images show an excess of power at the lowest modes, but no emission can be clearly localized to any one region of the sky. This image is highly suggestive that the most problematic foregrounds for 21cm EoR studies will not be easily identifiable bright sources, but rather an aggregate of fainter emission.

Subject headings: cosmology: observations — dark ages, reionization, first stars — techniques: interferometric

1. INTRODUCTION

The highly redshifted 21cm line of neutral hydrogen is widely regarded as one of the most promising probes of the high redshift universe, with potential to map out volumes extending from redshift ~ 1 through the Epoch of Reionization (EoR) to the dark ages at redshift 20 and beyond (for reviews of the field, see Furlanetto et al. 2006, Morales & Wyithe 2010, and Pritchard & Loeb 2012). Numerous facilities and experiments targeting the signal from the EoR are already online or under construction, including the LOW Frequency ARray (LOFAR; Yatawatta et al. 2013)¹¹, the Murchison Widefield Array (MWA; Tingay et al. 2012)¹², and the Donald C. Backer Precision Array for Probing the Epoch of Reionization (PAPER; Parsons et al. 2010)¹³. All 21cm cosmology experiments will need to separate bright galactic and extragalactic foregrounds from the neutral hydrogen signal, which can be fainter by as much as 5 orders of magnitude or more (see, e.g., Furlanetto et al. 2006 and Santos et al. 2005).

Considerable effort has been devoted to developing

schemes to remove or isolate foregrounds from 21cm data (e.g. Morales et al. 2006, Bowman et al. 2009, Liu et al. 2009, Liu & Tegmark 2011, Parsons et al. 2012b, Dillon et al. 2012). Almost all of these approaches rely on the spectral smoothness of foreground emission relative to the 21cm signal, which will contain significant structure versus frequency. The purpose of this letter is to use the delay transform technique presented in (Parsons et al. 2012b; hereafter, P12b) on observations from PAPER to test the behavior of actual foreground emission. We wish to understand the footprint of foregrounds in k -space to determine which modes of the 21cm power spectrum will be most accessible to observation. The structure of this letter is as follows: in §2, we describe the data used in these observations. In §3, we review the delay spectrum technique presented in P12b, and then describe the steps used in applying this approach to actual observations. We present our results in §4 and conclude in §5.

2. THE DATA

We use 4 hours of data collected in 10 second integrations between JD 2455747.48 and 2455747.64 (4 – 5 July 2011), using a 64 element PAPER array located on the SKA site in the Karoo region of South Africa. This data set comes from the same observing campaign described by Stefan et al. (2012), although this specific 4-hour window falls outside of the observations analyzed therein. The dipole antennas are arranged in a “minimum redundancy” configuration optimized for imaging analysis (Parsons et al. 2012a), which is shown in Figure 1. This configuration has a maximum baseline length of ~ 300 m, corresponding to an image plane resolution of 0.4° at 150 MHz. The PAPER correlator has a 100 MHz instantaneous bandwidth from 100 – 200 MHz divided into 2048 frequency channels. We correlate only one linear polarization on each dipole, and discard all data from

¹ Astronomy Dept., U. California, Berkeley, CA

² Dept. of Physics and Astronomy, U. Pennsylvania, Philadelphia, PA

³ Dept. of Electrical and Computer Engineering, U. Virginia, Charlottesville, VA

⁴ National Radio Astronomy Obs., Charlottesville, VA

⁵ Dept. of Astronomy, U. Virginia, Charlottesville, VA

⁶ National Radio Astronomy Obs., Socorro, NM

⁷ Radio Astronomy Lab., U. California, Berkeley, CA

⁸ School of Earth and Space Exploration, Arizona State U., Tempe, AZ

⁹ Square Kilometer Array, South Africa Project, Cape Town, South Africa

¹⁰ Cavendish Lab., Cambridge, UK

¹¹ <http://www.lofar.org/>

¹² <http://www.mwatelescope.org/>

¹³ <http://eor.berkeley.edu/>

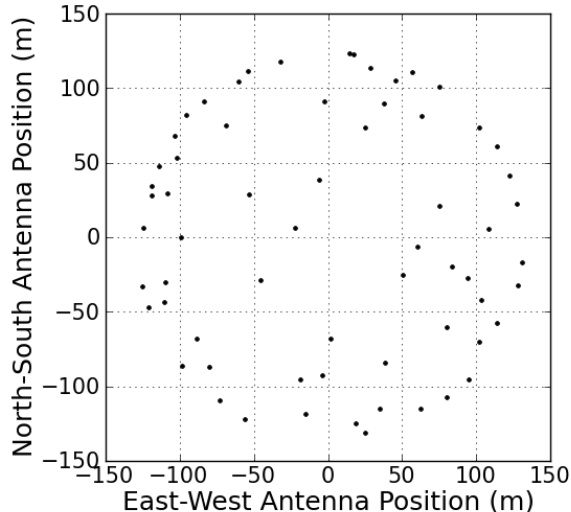


Figure 1. The configuration of the 64 PAPER dipoles used in this analysis. The zero-point is the center of the array. The y-axis is North/South, the x-axis is East/West, and distances are in meters.

antennas 40 and 55 which were cross-polarized.

An image of the field transiting during this time period is shown in Figure 2. This image spans 140 – 165 MHz; 100 sub-bands of 0.25 MHz were individually imaged and summed to make the map shown. No CLEANing or spectral slope correction was performed. The observation is centered on a low-foreground “cold patch,” a potential field for an EoR science observation. The Galactic plane, which is just setting at the end of the 4-hour observation, creates prominent sidelobes over the entire map.

Complex antenna based gains are derived using fringe-fitting to Centaurus A, Pictor A, and Fornax A; an overall gain scale is derived from the Helmboldt et al. (2008) source J2214-170. We perform a small gain linearization correction to mitigate data quantization effects in the correlator (described in Parsons et al. 2010) and a correction for temperature dependent gain drifts (described in Pober et al. 2012). We also perform radio-frequency interference (RFI) excision, manually flagging frequency channels of known transmitters, and flagging any points 6σ above the mean after differencing adjacent channels along the frequency axis.

3. ANALYSIS TECHNIQUES

At the core of our analysis is the delay spectrum technique presented in P12b. Since cosmological redshifting maps the observed 21cm line frequency into a distance measurement, the Fourier transform of the frequency axis are the k_{\parallel} line-of-sight modes of the 21cm power spectrum. However, this relation is clearly not true for foregrounds, where the frequency axis simply corresponds to the spectra of the sources. The delay transform first presented in Parsons & Backer (2009) provides a framework for mapping foreground emission into a cosmological k -space. The frequency Fourier transform of a single baseline’s visibility spectrum (the “delay transform”) maps celestial emission to “delay space,” where sources appear as Dirac delta functions, located at the delay in arrival time between the two elements of that baseline. These delays must be limited to values below the physi-

cal light travel time between the two antennas (the “horizon limit”), and so all emission from the sky maps to a region in the center of delay space determined only by the baseline length. However, any spectral structure in the visibilities acts as a convolving kernel in delay space. Foreground emission is spectrally smooth, translating into a narrow convolving kernel; 21cm emission has large amounts of spectral structure, and therefore its kernel scatters power from within the horizon limit to larger delays. P12b also showed that delay has a near one-to-one mapping to k_{\parallel} , meaning that those delay modes free from contaminating foreground emission are effective probes of the 21cm power spectrum. The baseline-length dependence creates better isolation on the shortest baselines, giving rise to the “wedge” structure seen in Datta et al. (2010), Vedantham et al. (2012), Morales et al. (2012), Trott et al. (2012), and P12b; we refer the reader to these works for more detailed and alternative derivations of the “wedge.”

3.1. Delay Space CLEAN

Some of the practical aspects of implementing the delay-spectrum approach in actual data were described in §3 of P12b. Of particular importance is the implementation of the frequency Fourier transform using a window function and the 1D-CLEAN algorithm first presented in Parsons & Backer (2009) to reduce the effects of RFI flags and band-edge effects. Even if foregrounds are spectrally smooth and easily localized in delay/ k_{\parallel} -space, such sharp edges in frequency space will introduce significant covariance in delay space, resulting in the scattering of foreground emission into otherwise uncontaminated regions of k -space. The 1D-CLEAN algorithm treats RFI flags as a sampling function in frequency space, and “fills in” these gaps by iteratively fitting the brightest Fourier components in the delay domain. As the sampling function is known exactly, this algorithm has proven extremely effective at removing covariance between delay modes. The end result is a model of our data which is free of RFI flagging gaps. We then form power spectra both of this model and the residuals between it and the raw data, before re-combining them. By separating the two components before the Fourier transform, we reduce the amount of power that can scatter off RFI gaps, minimizing bright sidelobes which would otherwise contaminate the EoR window in the power spectrum.

We force our foreground model to be smooth-spectrum in frequency by only allowing delay-space components which fall inside a baseline-dependent area (a “CLEAN box”), 50 ns beyond the physical maximum horizon delay on that baseline. This extra 50 ns allows the algorithm to model foreground emission pushed beyond the horizon limit. For this work, 50 ns appears to encompass enough foreground emission that the sidelobes of any remaining flux scattering off RFI gaps in the residuals are below the noise. Since our results do detect additional emission beyond our chosen cut-off, its exact value may need to be revisited in future analyses with more sensitivity.

3.2. Power Spectra

Once the data have been CLEANed, we form power spectra on a visibility-by-visibility basis. Our power spectrum estimates follow from equation (12) of

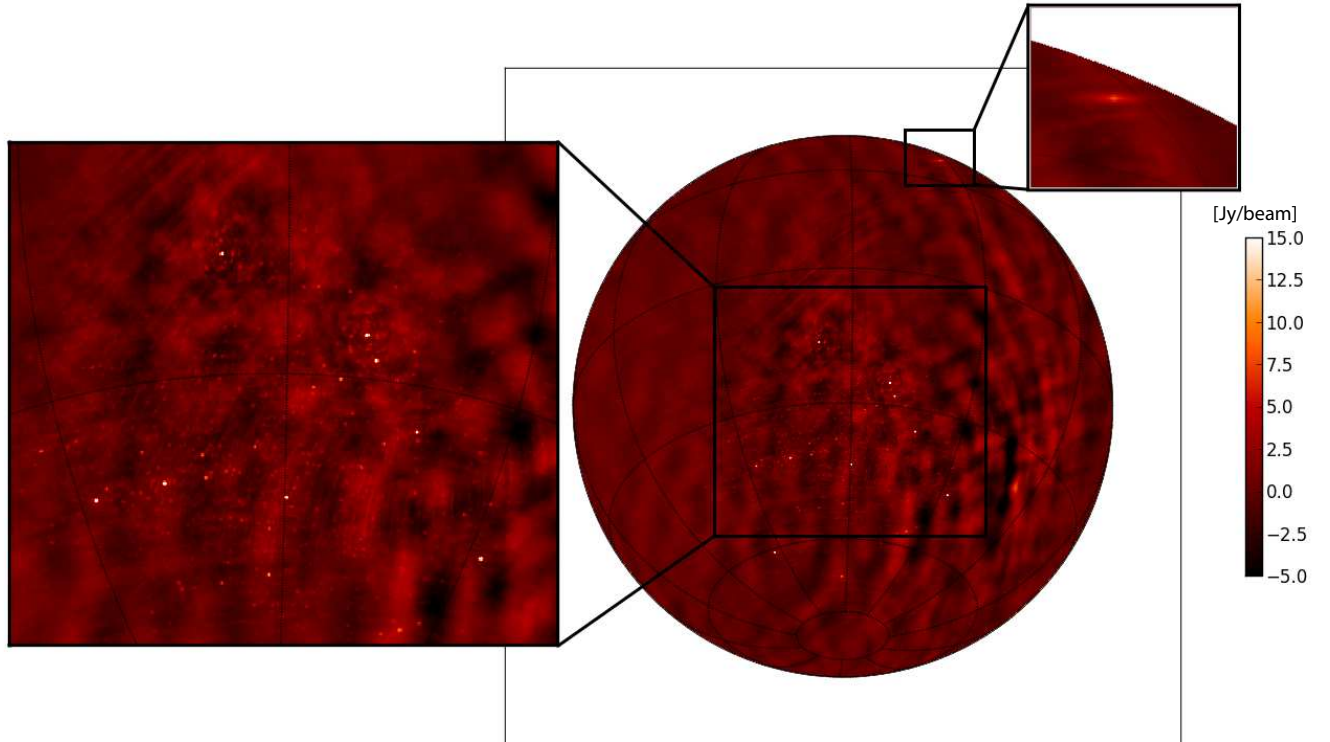


Figure 2. A dirty image of the data used in this analysis, centered on RA 21h52m and declination $-30^{\circ}43'$, the transiting zenith halfway through the observation. Prominent sidelobes from the Galaxy are seen in the right-hand side of the map. Close-ups show Cygnus A at 19h59m and $+40^{\circ}44'$ and the point source population of a potential EoR cold-patch. The color-scale is linear in Jy, with only the brightest point sources saturating the range.

Parsons et al. (2012a):

$$\hat{P}(k) \approx \tilde{V}_{21}^2 \left(\frac{\lambda^2}{2k_{\text{B}}} \right)^2 \frac{X^2 Y}{\Omega B}, \quad (1)$$

where λ is the observing frequency, k_{B} is Boltzmann’s constant, Ω is the solid angle of the primary beam,¹⁴ B is the observing bandwidth, X and Y are cosmological scalars which convert observed angles and frequencies into $h\text{Mpc}^{-1}$, and \tilde{V} is a delay transformed visibility. We avoid introducing a noise-bias by forming our estimator \tilde{V}_{21}^2 from adjacent time samples on a baseline. The 10-second interval between integrations is short enough that both measurements can be considered redundant samples of the same k -modes.

The isotropy of the universe allows us to then combine all power spectrum estimates \tilde{V}_{21}^2 in annuli of equal k_{\perp} to form a 2D power spectrum in the $(k_{\perp}, k_{\parallel})$ -plane. We note that the method used here does not take advantage of any coherent integration within a uv -pixel. Since foreground emission dominates the observed signal, the

¹⁴ Derivations of equation 1 in Morales (2005), McQuinn et al. (2006), and Parsons et al. (2012a), relate ΩB to an effective cosmological volume, using a top-hat primary beam or effective area as a pedagogical tool to simplify the result. More generally, however, the effective Ω in equation 1 is actually $\int A^2(\theta, \phi) d\theta d\phi$, where $A(\theta, \phi)$ is the power response of the primary beam. A derivation of this effect will be presented in a subsequent full length publication by Parsons et al. For PAPER, this beam is a factor of ~ 2 smaller than $\int A(\theta, \phi) d\theta d\phi$.

loss of sensitivity is not important, and we ignore this effect for computational efficiency. For EoR science runs, however, PAPER explicitly focuses on maximizing the sensitivity boost from coherent integration, using “maximum redundancy” configurations designed to sample select uv -pixels for long periods of time.

4. RESULTS

To make power spectra of the 4-hour dataset described above, we first run our CLEAN algorithm over the full 100 MHz band. Using the whole band gives the best resolution in delay space, and since foregrounds are nearly coherent over the whole band, the additional information gives CLEAN the most signal-to-noise to build its model. For the cosmological delay transform to make power spectra, we use only a 25 MHz band from 140 to 165 MHz. This smaller band still exceeds the ~ 8 MHz band over which the $z \sim 8$ universe can be treated as coeval (Furlanetto et al. 2006). Since the main purpose of this work is to understand the k -space behavior of foregrounds, we ignore this effect, as the additional bandwidth gives us better k -space resolution.

Forming individual power spectra from each baseline of the array and binning in $|k_{\perp}|$ yields the 2-dimensional $P(k_{\perp}, k_{\parallel})$ shown in Figure 3. The k_{\perp} -axis is binned with a resolution of $1.87 \times 10^{-4} h\text{Mpc}^{-1}$; gaps are visible where there are no baselines of that length. We do no binning in k_{\parallel} ; this resolution is set by the 25 MHz

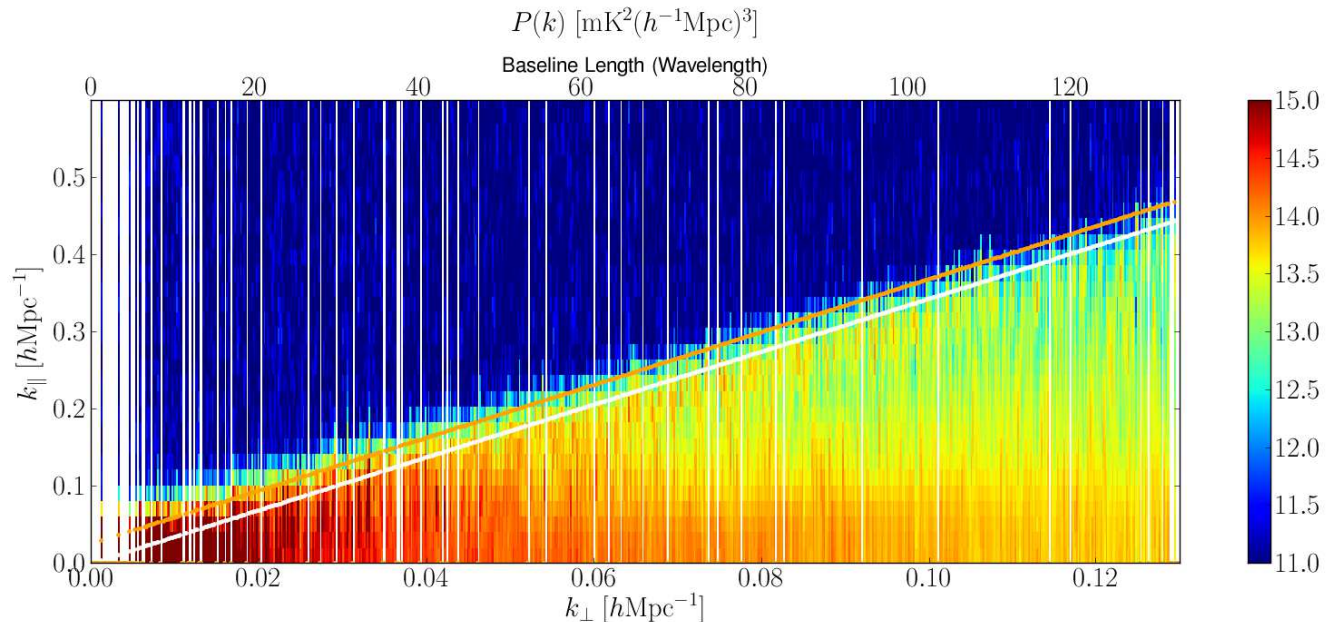


Figure 3. A two-dimensional power spectrum of the 4 hours of data analyzed. The wedge-like nature of the foreground emission is clear. The white line marks the horizon limit and the orange line is 50 ns beyond. The colorscale is logarithmic and the units are $\text{mK}^2 (h^{-1}\text{Mpc})^3$. The binning is described in the text.

bandwidth used in the analysis.¹⁵ The most prominent feature is the “wedge”-like shape of the foreground emission as predicted. As argued in P12b, this “wedge” footprint in k -space is not a result of imperfect calibration in foreground removal (since we attempt no foreground removal in this work), but a property of the emission itself as measured by an interferometer.

The white diagonal line in Figure 3 corresponds to the horizon-limit in k_{\parallel} for a baseline of corresponding length k_{\perp} ; the orange line is 50 ns beyond the horizon, inside of which we allowed Fourier components in the deconvolution described in §3.1. As predicted, emission extends beyond the horizon limit due to the intrinsic spectral structure of the foreground emission.

We draw attention to the fact that the supra-horizon emission does not have a constant width in k_{\parallel} as a function of k_{\perp} . Rather, more emission extends beyond the horizon on the smallest k_{\perp} -values (i.e. the shortest baselines). We expect this behavior to result from two different effects. First, the shortest baselines will resolve out less of the diffuse Galactic synchrotron, so that the emission will be brighter. Therefore, we can see its sidelobes extend further in k_{\parallel} before they fall below the noise level. The second effect is somewhat more subtle and can be best illustrated with an example. Consider two east-west baselines of length 10 and 100λ at 150 MHz, which correspond to light travel times (i.e. horizon limits) of 66.7 and 667 ns, respectively. A point source 20° above the eastern horizon corresponds to geometric delays of 62.6 and 626 ns on these baselines. If the source spectrum has a given amount of “unsmoothness” and creates a delay space kernel of width 10 ns, then this kernel, centered at the geometric delay of the source, will lead to emission beyond the horizon on the 10λ baseline, but not on the

100λ baseline. This example illustrates how the same sources of emission will naturally lead to more corruption of supra-horizon delays on shorter baselines than on longer ones.

Finally, we draw attention to the “edge brightening” of the foreground emission in the wedge on the longest baselines as one moves near the horizon limit. This feature can be attributed to the Galactic plane, and moves as expected when the data are viewed as a function of time.

To highlight the steepness of the foreground roll-off, we plot 1-dimensional k_{\parallel} power spectra for bins of several baseline lengths in Figure 4. We see that the foreground emission can fall by as much as three to four orders of magnitude in a factor of 2 change in k_{\parallel} . It is difficult to explicitly compare this result to the predictions of P12b, due to the different resolutions and binning used. The placement of bin edges can significantly complicate comparison when the fall-off is so steep, as a slight shift in the bin can result in a large change in the average value within. For similar reasons, it is difficult to say exactly where the emission falls below the noise. Given these caveats, there is nothing in these data to contradict P12b. It is clear, however, that sensitivities will have to increase significantly before anything can be said about the behavior of foreground emission at the tens of mK^2 level where the expected EoR signal lies.

To both demonstrate the effectiveness of the delay-space foreground isolation and to further investigate the nature of the supra-horizon emission, we high-pass filter the data in delay-space, selecting only delay modes more than 50 ns beyond the horizon limit, i.e., we select the emission lying beyond the orange line in Figure 3. We then image this data from 140 to 165 MHz in one-hundred 0.25 MHz bins to form a data-cube versus frequency. Finally, we Fourier transform our data-cube versus frequency to create maps of individual k_{\parallel} modes. Three of the resultant maps for $k_{\parallel} = 0.06, 0.08,$

¹⁵ Because of the Blackman-Harris window function used in CLEAN, only every other sample plotted in k_{\parallel} is statistically independent.

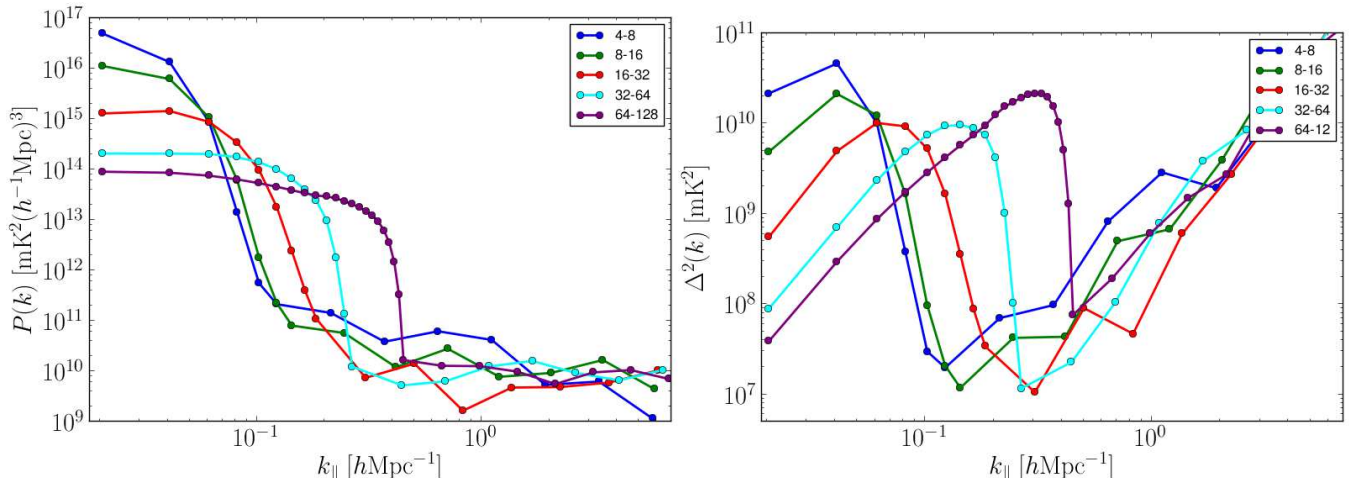


Figure 4. Left: A 1-dimensional power spectrum versus k_{\parallel} for bins of several baseline lengths. To preserve the steep roll-off of the foreground emission, the data are plotted with their natural resolution at lower k_{\parallel} values, and logarithmically binned at higher values. Right: The same as the left, but the dimensionless power spectrum $\Delta^2(k) = \frac{k^3}{2\pi^2} P(k)$.

and $0.51 h\text{Mpc}^{-1}$ are shown in Figure 5.

The flux scale in these images has been reduced by 2 to 3 orders of magnitude from Figure 2, demonstrating the effectiveness of delay-space filtering. Interpreting the flux scale in the lowest k_{\parallel} modes is complicated, since most of baselines at these modes have been filtered off, whereas, the $k_{\parallel} = 0.51 h\text{Mpc}^{-1}$ mode is effectively a noise map. It can be seen in Figure 3 that this mode lies above the wedge, and therefore nothing has been filtered from it. The RMS in this map (calculated from the complex data) is 14 mJy. We can estimate the expected noise level using:

$$\Delta\sigma = \frac{2k_B\Omega}{\lambda^2} \frac{T_{\text{sys}}}{\sqrt{N(N-1)Bt}}, \quad (2)$$

where k_B is Boltzmann’s constant, Ω is the solid angle of the primary beam, λ is the observing wavelength, T_{sys} is the system temperature, N is the number of antennas in the array, B is the bandwidth, and t is the observing time (Thompson et al. 2007). For this observation $\Omega = 0.75$ sr, $t = 4$ hours, $\lambda = 1.96$ m, $B = 25$ MHz, and $T_{\text{sys}} = 1000$ K. This somewhat high value for T_{sys} is reasonable given the Galactic emission in these observations; the values of T_{sys} for PAPER will be presented in a forthcoming publication by Parsons et al. Using these values gives an expected RMS of 14 mJy, in accord with our measurement.

The $k_{\parallel} = 0.06$ and $0.08 h\text{Mpc}^{-1}$ maps are clearly not noise dominated. Accounting for the noise that was removed by filter, these data have rough “effective” RMS values of 35 mJy, well in excess of our noise estimate. Given the presence of emission in these modes above the orange line in Figure 3, it is not surprising that we see excess power. What is surprising is that none of this emission can be easily associated with the brightest sources or structures visible in Figure 2. Rather, it appears that the bulk of the emission contaminating the EoR window comes from an aggregate of fainter emission. One might be concerned that emission can leak from lower k_{\parallel} bins into the modes shown, but as argued in §3.1, our deconvolution algorithm is extremely effective at eliminating this

covariance. However, we caution the reader against interpreting these maps as images of true coherent structures on the sky. The fact that the spatial pattern of emission changes significantly from $k_{\parallel} = 0.06$ to $0.08 h\text{Mpc}^{-1}$ suggests the emission is a diffuse background and our images are limited by sidelobes.

We note one additional interesting feature in these maps. The noise-dominated $k_{\parallel} = 0.51 h\text{Mpc}^{-1}$ gives a good impression of the PAPER primary beam shape. In the 0.06 and $0.08 h\text{Mpc}^{-1}$ maps, however, bright emission extends well beyond the half-power point of the beam (roughly 45° FWHM). Under the lens of the delay transform, one suspects that the emission closest to the horizon can most easily create supra-horizon emission. These images show that while emission from well outside the beam FWHM contributes significantly to the supra-horizon emission, the PAPER primary beam roll-off is enough to keep this pattern from extending all the way out the edge of the image.

5. CONCLUSIONS

We have presented new observations from PAPER measuring the properties of foreground emission in cosmological Fourier space. These observations have confirmed general predictions presented in, e.g., Datta et al. (2010), Morales et al. (2012) and P12b: that foreground emission occupies a “wedge” in the 2D $(k_{\perp}, k_{\parallel})$ plane, leaving a window at higher k_{\parallel} values for 21cm EoR studies. We have also confirmed that shorter baselines yield a larger window onto the cosmological signal. However, this the window does not grow perfectly linearly with decreasing baseline length. Therefore, while shorter baselines do make the best probes of the EoR signal, there will be diminishing returns at the shortest baselines. We have also presented an images of several k_{\parallel} modes of “unsmooth” emission extending past the nominal edge of the wedge. These images are unable to localize any of the emission to known sources on the sky, suggesting that the most problematic foregrounds for EoR observations are a diffuse background.

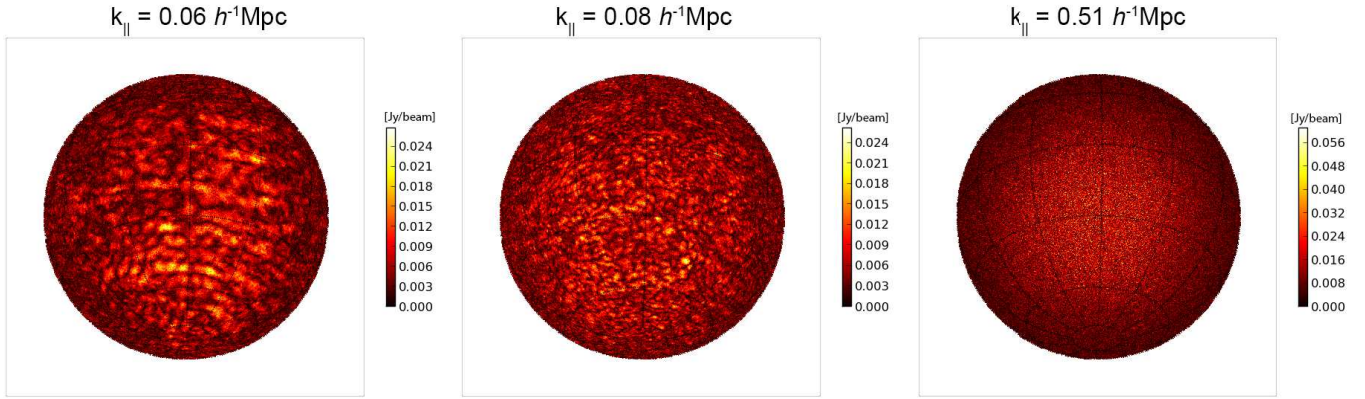


Figure 5. Images of the magnitude of select k_{\parallel} modes in the data, after a high-pass delay space filter has removed all emission interior to 50 ns beyond the horizon limit (i.e. emission below the orange line in Figure 3 has been removed). The color-scale is linear in Jy, although the flux scale on the lowest k_{\parallel} -modes is compromised due to the filter. While emission is clearly present in the low k_{\parallel} modes, it cannot be identified with the bright sources in Figure 2, nor are the features obviously correlated with Galactic structure.

We would like to thank our reviewer for their thoughtful and helpful comments. We thank SKA-SA for their efforts in ensuring the smooth running of PAPER. PAPER is supported through the NSF-AST program (awards 0804508, 1129258, and 1125558), the Mt. Cuba Astronomical Association, and by significant efforts by staff at NRAO.

REFERENCES

- Bowman, J. D., Morales, M. F., & Hewitt, J. N. 2009, *ApJ*, 695, 183
- Datta, A., Bowman, J. D., & Carilli, C. L. 2010, *ApJ*, 724, 526
- Dillon, J. S., Liu, A., & Tegmark, M. 2012, arXiv:1211.2232
- Furlanetto, S. R., Oh, S. P., & Briggs, F. H. 2006, *Phys. Rep.*, 433, 181
- Helmboldt, J. F., Kassim, N. E., Cohen, A. S., Lane, W. M., & Lazio, T. J. 2008, *ApJS*, 174, 313
- Liu, A., & Tegmark, M. 2011, *Phys. Rev. D*, 83, 103006
- Liu, A., Tegmark, M., Bowman, J., Hewitt, J., & Zaldarriaga, M. 2009, *MNRAS*, 398, 401
- McQuinn, M., Zahn, O., Zaldarriaga, M., Hernquist, L., & Furlanetto, S. R. 2006, *ApJ*, 653, 815
- Morales, M. F. 2005, *ApJ*, 619, 678
- Morales, M. F., Bowman, J. D., & Hewitt, J. N. 2006, *ApJ*, 648, 767
- Morales, M. F., Hazelton, B., Sullivan, I., & Beardsley, A. 2012, *ApJ*, 752, 137
- Morales, M. F., & Wyithe, J. S. B. 2010, *ARA&A*, 48, 127
- Parsons, A., Pober, J., McQuinn, M., Jacobs, D., & Aguirre, J. 2012a, *ApJ*, 753, 81
- Parsons, A. R., & Backer, D. C. 2009, *AJ*, 138, 219
- Parsons, A. R., Pober, J. C., Aguirre, J. E., Carilli, C. L., Jacobs, D. C., & Moore, D. F. 2012b, *ApJ*, 756, 165
- Parsons, A. R., et al. 2010, *AJ*, 139, 1468
- Poher, J. C., et al. 2012, *AJ*, 143, 53
- Pritchard, J. R., & Loeb, A. 2012, *Reports on Progress in Physics*, 75, 086901
- Santos, M. G., Cooray, A., & Knox, L. 2005, *ApJ*, 625, 575
- Stefan, I. I., et al. 2012, arXiv:1212.1624
- Thompson, A. R., Moran, J. M., & Swenson, G. W. 2007, *Interferometry and Synthesis in Radio Astronomy*, John Wiley & Sons, 2007.
- Tingay, S. J., et al. 2012, arXiv:1206.6945
- Trott, C. M., Wayth, R. B., & Tingay, S. J. 2012, *ApJ*, 757, 101
- Vedantham, H., Udaya Shankar, N., & Subrahmanyan, R. 2012, *ApJ*, 745, 176
- Yatawatta, S., et al. 2013, arXiv:1301.1630